How to cite: *Angew. Chem. Int. Ed.* **2024**, *63*, e202405459
doi.org/10.1002/anie.202405459

Electrocatalytic NH_3 Production

Ultralow Catalytic Loading for Optimised Electrocatalytic Performance of AuPt Nanoparticles to Produce Hydrogen and Ammonia

Leticia S. Bezerra[+], Paul Brasseur[+], Sam Sullivan-Allsop, Rongsheng Cai, Kaline N. da Silva, Shiqi Wang, Harishchandra Singh, Ashok K. Yadav, Hugo L. S. Santos, Mykhailo Chundak, Ibrahim Abdelsalam, Vilma J. Heczko, Elton Sitta, Mikko Ritala, Wenyi Huo, Thomas J. A. Slater, Sarah J. Haigh,* and Pedro H. C. Camargo**

Abstract: The hydrogen evolution and nitrite reduction reactions are key to producing green hydrogen and ammonia. Antenna–reactor nanoparticles hold promise to improve the performances of these transformations under visible-light excitation, by combining plasmonic and catalytic materials. However, current materials involve compromising either on the catalytic activity or the plasmonic enhancement and also lack control of reaction selectivity. Here, we demonstrate that ultralow loadings and non-uniform surface segregation of the catalytic component optimize catalytic activity and selectivity under visible-light irradiation. Taking Pt–Au as an example we find that fine-tuning the Pt content produces a 6-fold increase in the hydrogen evolution compared to commercial Pt/C as well as a 6.5-fold increase in the nitrite reduction and a 2.5-fold increase in the selectivity for producing ammonia under visible light excitation relative to dark conditions. Density functional theory suggests that the catalytic reactions are accelerated by the intimate contact between nanoscale Pt-rich and Au-rich regions at the surface, which facilitates the formation of electron-rich hot-carrier puddles associated with the Pt-based active sites. The results provide exciting opportunities to design new materials with improved photocatalytic performance for sustainable energy applications.

Introduction

Efficient synthesis of green hydrogen and ammonia is key to a sustainable energy future.[1,2] The conversion of nitrite/nitrate to ammonia holds promise as a greener alternative to the energy intensive Haber–Bosch process, as ammonia serves as an efficient and carbon-free energy carrier.[3] While ammonia is a typical feedstock for nitrate synthesis, the conversion of nitrite/nitrate to ammonia enables environmental remediation as ammonia is less harmful in aquatic environments compared to nitrite/nitrate.[4] Green hydrogen and ammonia can be produced by the hydrogen evolution and nitrate/nitrite reduction reactions, respectively,[2,5] but improved catalysts are urgently needed to improve the activity for both transformations and increase the selectivity for the formation of ammonia.[6–9] Plasmonic catalysis has the potential to address both of these challenges by enabling the use of sunlight as a primary energy input to drive these

[*] L. S. Bezerra,[+] P. Brasseur,[+] K. N. da Silva, S. Wang, H. L. S. Santos, M. Chundak, I. Abdelsalam, V. J. Heczko, M. Ritala, P. H. C. Camargo
Department of Chemistry, University of Helsinki, A.I. Virtasen aukio 1, PO Box 55, FIN-0014 Helsinki, Finland
E-mail: pedro.camargo@helsinki.fi

S. Sullivan-Allsop, R. Cai, S. J. Haigh
Department of Materials, University of Manchester, Manchester M13 9PL, United Kingdom
E-mail: sarah.haigh@manchester.ac.uk

H. Singh
Nano and Molecular Systems Research Unit, University of Oulu, Oulu FIN-90014, Finland

A. K. Yadav
Synchrotron SOLEIL Beamline SIRIUS, Saint-Aubin, F-91192, Gif sur Yvette, France

E. Sitta
Department of Chemistry, Federal University of Sao Carlos, Rod. Washington Luis, km 235, Sao Carlos, 13565-905, Brazil

W. Huo
College of Mechanical and Electrical Engineering, Nanjing Forestry University. Nanjing, 210037, P. R. China
E-mail: wyhuo@njfu.edu.cn

W. Huo
NOMATEN Centre of Excellence, National Centre for Nuclear Research, Otwock, 05-400, Poland

T. J. A. Slater
Cardiff Catalysis Institute, School of Chemistry, Cardiff University, Cardiff, CF10 3AT, United Kingdom

[+] These authors contributed equally to this work

reactions.[10–12] Enhanced reaction rates are achieved because of the light-driven localized surface plasmon resonance (LSPR) excitation of plasmonic nanoparticles (NPs), which leads to the generation of hot carriers (hot electrons and holes) and localized heating; accelerating catalytic reactions.[13–16] However, plasmonic catalysts suffer from poor reaction selectivity, which has prevented their wide uptake for sustainable energy applications[17–19]

Bimetallic antenna–reactor NPs, that incorporate both plasmonic metal (antenna) and catalytic metals (reactor), are at the forefront of plasmonic catalysis.[20,21] The plasmonic component harvests light energy through LSPR excitation, which generates LSPR-excited charge carriers that can enhance the catalytic performance of the catalytic metal component.[11,22,23] However, the challenges with antenna–reactor NPs are to retain the plasmonic properties when the catalytic metal is added[24–26] and to improve catalytic metal utilization, which is important for costly Pt-group metals.[27–29]

Here we report on bimetallic antenna-reactor AuPt NPs prepared by depositing ultralow loadings of Pt on the surface of Au NPs to combine catalytic and plasmonic properties (from Pt and Au, respectively). By using low concentrations of the catalytic material, we aim to prevent a significant decrease in the optical absorption of Au and optimize catalytic Pt metal utilization and performance. Our results reveal the formation of an uneven bimetallic AuPt shell at the surface of the Au NPs, in which the Pt distribution became more dilute as the Pt content decreased. Taking the hydrogen evolution and nitrite reduction reactions (HER and NO_2RR, respectively) as key target catalytic transformations, we found that the control over the Pt distribution in the AuPt NPs could significantly improve both catalytic activity and reaction selectivity under visible light excitation compared to a commercial Pt/C catalyst. Density functional theory is applied to reveal mechanistic insights into why the lowest catalytic loading (0.6 at % Pt) gives the best photocatalytic performance.

Results and Discussion

The synthesis of the AuPt NPs is shown in Scheme 1. This yielded bimetallic NPs containing 6 and 0.6 at % Pt (named $Au_{94}Pt_6$ and $Au_{99.4}Pt_{0.6}$ NPs, respectively), as determined by atomic emission spectroscopy (AES, Table S1). We aimed to keep the Pt content in the NPs as low as possible, ideally below 10 at %, to maximize Pt use and enable strong optical properties from Au. In this case, 6 at % of Pt was chosen as the highest composition in terms of Pt because it corresponds to the estimated concentration to achieve a monolayer Pt deposition on the Au surface, assuming the formation of an Au@Pt core–shell NP. In terms of the lower Pt concentrations, 0.6 at % was chosen as it corresponds to submonolayer coverage and to the regime in which single-atom alloys could form.

Figure 1A–G shows transmission electron microscope (TEM) images, high angle annular dark field (HAADF)

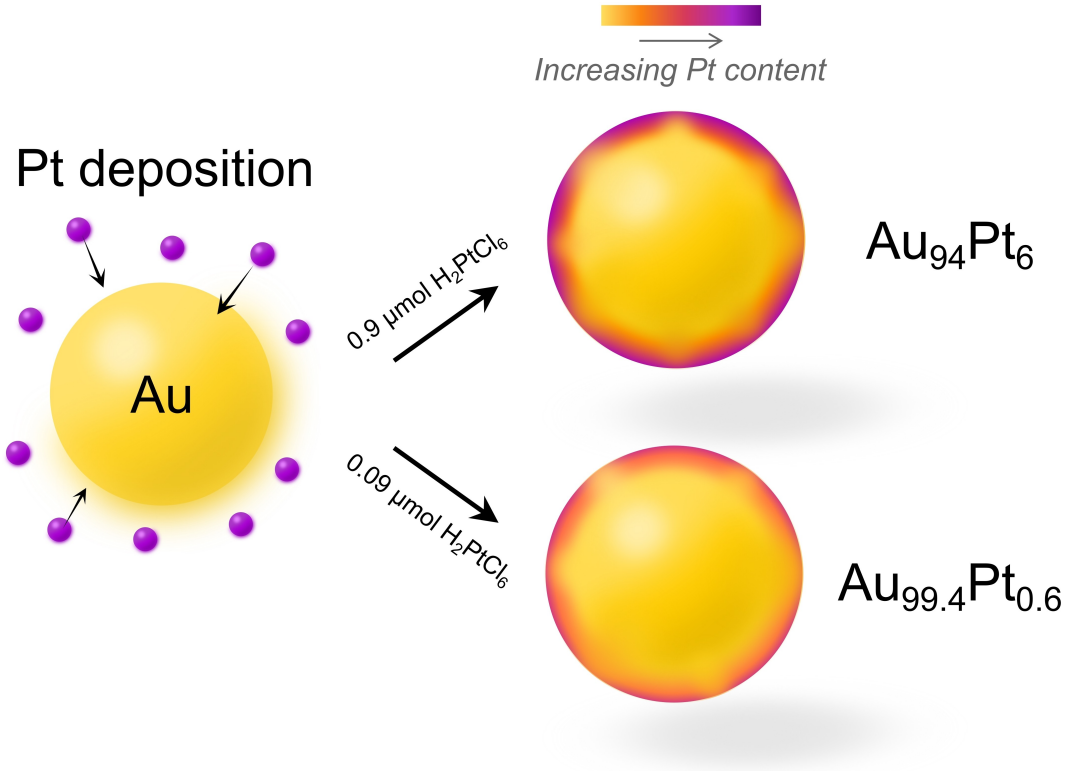

Scheme 1. Approach for the synthesis of $Au_{94}Pt_6$ and $Au_{99.4}Pt_{0.6}$ NPs. By employing Au NPs as seeds, Pt deposition was performed using H_2PtCl_6 as the precursor and L-ascorbic acid as the reducing agent.

scanning transmission electron microscope (STEM) images, STEM energy dispersive X-ray (STEM-EDX) elemental maps, and EDX elemental line scans for $Au_{94}Pt_6$ and $Au_{99.4}Pt_{0.6}$ NPs. The TEM images for both $Au_{94}Pt_6$ and $Au_{99.4}Pt_{0.6}$ NPs (Figure 1A and D, respectively) demonstrate that the NPs have a spherical shape. Both particle size distributions were relatively monodisperse with similar mean diameters of 13 ± 2 nm and 12 ± 2 nm for $Au_{94}Pt_6$ and $Au_{99.4}Pt_{0.6}$ NPs, respectively. No changes in size or shape relative to the initial Au NPs were detected after Pt deposition. Atomic resolution imaging of $Au_{94}Pt_6$ and $Au_{99.4}Pt_{0.6}$ NPs (Figure 1B and E, respectively) shows the NPs have relatively smooth surfaces, indicative that Pt is not present as protruding surface islands. Au and Pt are very similar in atomic number ($Z = 79$ and $Z = 78$ respectively) so cannot be accurately distinguished using Z-contrast HAADF STEM imaging. Thus, STEM-EDX analysis was conducted to obtain the distribution of elements within the samples, as shown in Figures 1C and F for $Au_{94}Pt_6$ and $Au_{99.4}Pt_{0.6}$ NPs, respectively. EDX quantification is generally only recommended for elemental concentrations of greater than 0.1 at % and for Pt and Au quantification, there is the additional challenge of the very close proximity of the Au and Pt characteristic X-ray peaks. To overcome the limitations of conventional EDX data processing methods which typically only consider the relative intensities of single X-ray emission peaks, here we included all available Au and Pt X-ray signals in the model fitting together with a background window subtraction optimized for the specific elements present in the NPs (see Supporting Information and Figures S1–S3 for more details). This approach provided mean compositions of 91.9 at % Au, 8.1 at % Pt for $Au_{94}Pt_6$ NPs, and 97.8 at % Au, 2.2 at % Pt for $Au_{99.4}Pt_{0.6}$ NPs with relatively small standard deviation errors of 1.2 at % and 0.5 at % (Figure S4). The individual STEM-EDX elemental maps showed that all the NPs had a Pt-enriched surface shell (Figure 1B–F, Figures S5 and S6) with examination of extracted line-scan elemental profiles revealing similar Pt-rich shell thicknesses of 1.33 nm for $Au_{94}Pt_6$ and 1.38 nm for $Au_{99.4}Pt_{0.6}$.

Electron energy loss spectroscopy (EELS) analysis was further utilized to characterize the surface Pt enrichment of $Au_{94}Pt_6$ NPs with a non-negative matrix factorization (NMF) approach being required to obtain any information about the Pt distribution from the features in the spectra (Figure 1H and I). NMF revealed one component that is dominated by a spectral feature at the location of the Pt K edge, and this was found to be strongly localized at the NP surface; providing further verification of the presence of a ~1 nm thick Pt-rich surface shell. EELS has a much lower relative sensitivity towards heavier elements than EDX,[30] hence only the higher Pt content, $Au_{94}Pt_6$, nanoparticles were able to achieve a detectable Pt EELS signal (Figure 1J). The high-loss EELS spectra reconstructed from the 2 dominant NMF components for the shell region (red line) shown in Figure 1J revealed the Pt edge and a shift in the Au edge.[31]

If we consider all the Pt in the NPs to be contained in a homogeneous shell with a thickness of 1.3 nm, a simple geometric model in combination with our STEM-EDX quantification of individual particles gives a mean composition for the shell of 16.3 at % Pt for $Au_{94}Pt_6$ and 4.0 at % Pt for $Au_{99.4}Pt_{0.6}$. However, high magnification EDX and EELS elemental mapping of the NP surfaces shows that, although the surface is smooth and no visible disruption in the local crystal structure is observed at atomic resolution (both Pt and Au are expected to adopt the face-centred cubic crystal lattice), the elemental distribution of the shell is not homogeneous and consists of uneven compositional patches with higher and lower Pt. Point analysis on the data in Figure 1C shows nanoscale regions in the shell have local Pt contents as high as 90 at % and as low as 5 at %. UV/Vis, XPS, Synchrotron XRD, XANES, and EXAFS data (see Supporting Information Figure S7 and Table S2 for more details) support these observations on the formation of an AuPt alloy on the surface of the NPs, which decreases in Pt concentration as the overall Pt content in the NPs decreases.

We assessed the hydrogen evolution reaction (HER) performance of $Au_{99.4}Pt_{0.6}$ and $Au_{94}Pt_6$ NPs both in the dark and when illuminated with light (525 nm wavelength, 58.50 $mW\,cm^{-2}$) and compared the results to those of a commercial Pt/C catalyst (Figure S8, Pt NPs were 2 nm in diameter, containing 20 wt % Pt on C). The linear sweep voltammetry (LSV) plots normalized by Pt mass are presented in Figure 2A and the mass activities at −0.1 V are shown in Figure 2B. In the dark, the $Au_{94}Pt_6$ NPs displayed comparable mass activity to the Pt/C catalyst, while the $Au_{99.4}Pt_{0.6}$ NPs displayed significantly higher mass activity, with an enhancement of 6- and 5-fold, relative to $Au_{94}Pt_6$ and Pt/C NPs, respectively. The corresponding mass activity values were also much better for $Au_{99.4}Pt_{0.6}$, at 6.1, 1, and 1.1 $A\,mg^{-1}_{Pt}$ for $Au_{99.4}Pt_{0.6}$, $Au_{94}Pt_6$ and Pt/C NPs, respectively. These results suggest that achieving an ultra-low loading of Pt at the Au NP surface was crucial for optimizing the HER activity even without LSPR excitation. We also prepared two more catalyst samples with a smaller Pt content relative to $Au_{99.4}Pt_{0.6}$: $Au_{99.7}Pt_{0.3}$ and $Au_{99.9}Pt_{0.1}$. The LSV plots (Figure S9A) and overpotential values at $-10\,mA\,cm^{-2}$ (Figure S9B) demonstrate a decline in the catalyst's activity due to the decrease in Pt content following the order: $Au_{99.4}Pt_{0.6} > Au_{99.7}Pt_{0.3} > Au_{99.9}Pt_{0.1}$.

LSPR excitation produced higher current densities relative to dark conditions for all catalysts (Figure 2A and S10A–C), with the greatest enhancement seen for the best-performing catalyst in dark conditions ($Au_{99.4}Pt_{0.6}$ NPs). Indeed, the mass activity for $Au_{99.4}Pt_{0.6}$ NPs with LSPR excitation reached 7 $mA\,\mu g^{-1}_{Pt}$ (Figure 2B), 7- and 6-fold higher than $Au_{94}Pt_6$ and Pt/C NPs, respectively (Table S3 presents a comparison with other reported Pt-based systems). The mass activities in terms of the total metal loading are shown in Figure S11. In this case, the samples display lower catalytic activity relative to Pt. It is important to note, however, that Au is not catalytic active for the HER, and it acts as an antenna for light absorption and support for the Pt active sites in the AuPt NPs. The electrochemical active surface area (ECSA) and ECSA normalized current density curves are shown in Figure S12. The ECSA-normalized current density confirms the higher catalytic activity of

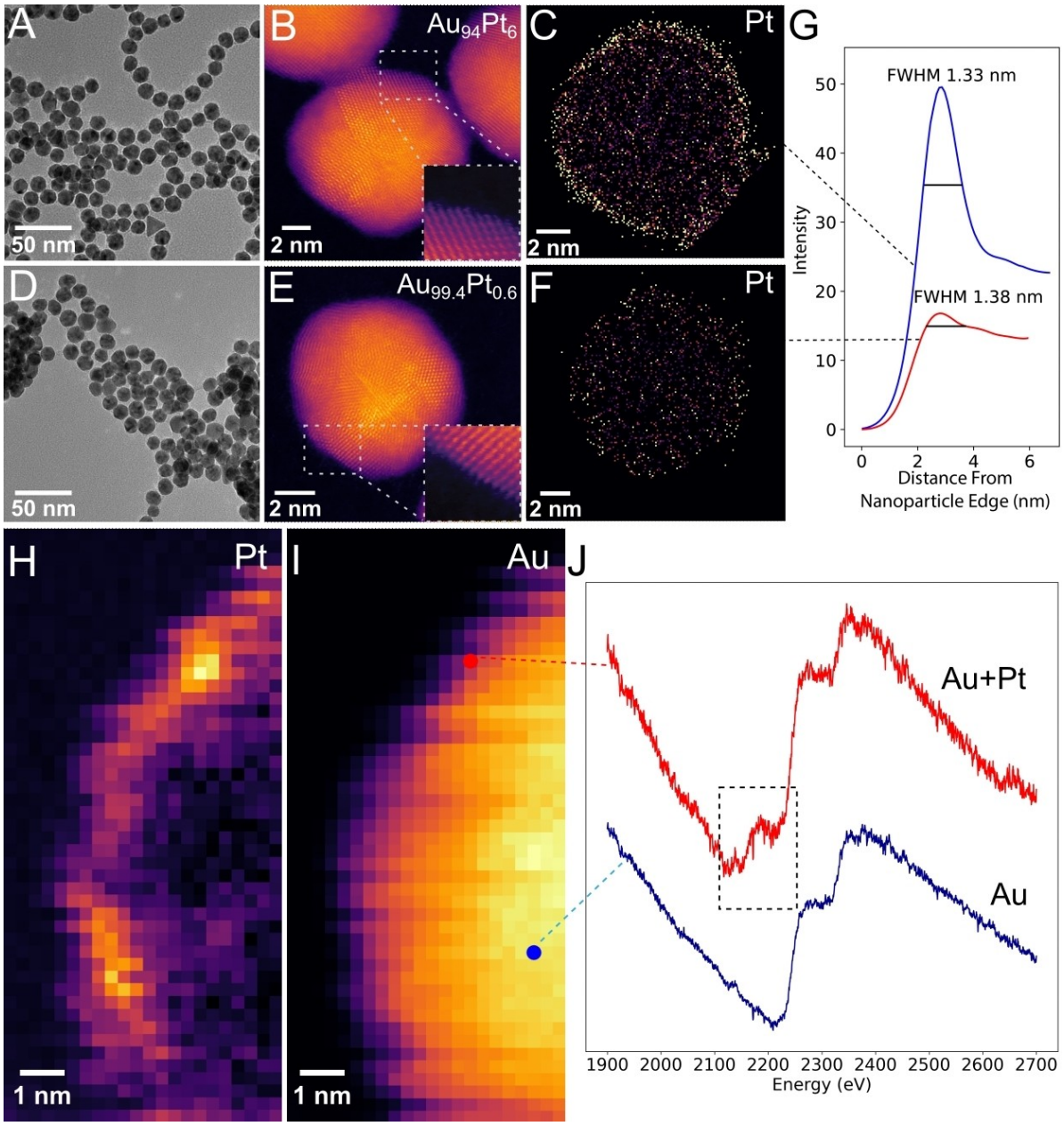

Figure 1. Characterization of elemental distribution in $Au_{94}Pt_6$ and $Au_{99.4}Pt_{0.6}$ NPs. (A and D) TEM and (B and E) STEM-HAADF images with an inset showing a zoom-in of the nanoparticle surface, (C and F) STEM-EDX elemental maps for Pt for (A–C) $Au_{94}Pt_6$ and (D–F) $Au_{99.4}Pt_{0.6}$ NPs, respectively. (G) EDX radially averaged line scans for $Au_{94}Pt_6$ (red trace) and $Au_{99.4}Pt_{0.6}$ (blue trace) NPs from the nanoparticles highlighted in purple in (C) and (F), respectively. (H and I) EELS decomposition component mapping and (J) NMF 2-component reconstructed high-loss EELS spectra for the core and shell locations identified in $Au_{94}Pt_6$. The Au EELS component contributes 90% of the signal.

$Au_{99.4}Pt_{0.6}$ relative to $Au_{94}Pt_6$ and Pt/C (ECSA-normalized activity follows the order: $Au_{99.4}Pt_{0.6} > Au_{94}Pt_6 > Pt/C$). Figure S13 shows the HER light intensity and wavelength dependence for $Au_{99.4}Pt_{0.6}$ NPs. While an increase in activity was detected as a function of the light intensity, the variations in terms of the wavelength were not significant.

The HER mechanism in acidic media can be described by the Volmer, Heyrovsky, and Tafel steps (eq. 1–3).[32] The Tafel diagrams (Figure 2C) give a Tafel slope of 42 mV dec^{-1} for $Au_{99.4}Pt_{0.6}$ as compared to 30 mV dec^{-1} for $Au_{94}Pt_6$ and Pt/C. This indicates that, while the Tafel step is rate-limiting in a Volmer–Tafel mechanism for $Au_{94}Pt_6$ and Pt/C NPs, the Heyrovsky step in a Volver-Heyrovsky mechanism becomes rate-limiting for the $Au_{99.4}Pt_{0.6}$ NPs probably due to the low H_{ad} surface coverage. Moreover, the Pt–H_{ad} binding energy could differ in $Au_{99.4}Pt_{0.6}$ compared to pure Pt NPs due to the reduction in the Pt–Pt coordination number when the Pt concentration at the surface is lowered (as supported by our DFT calculations described below), leading to the higher mass activity observed for HER in the dark. Finally, the presence of Pt–O surface sites in $Au_{99.4}Pt_{0.6}$ as evidenced by our spectroscopic data can also contribute to the improved

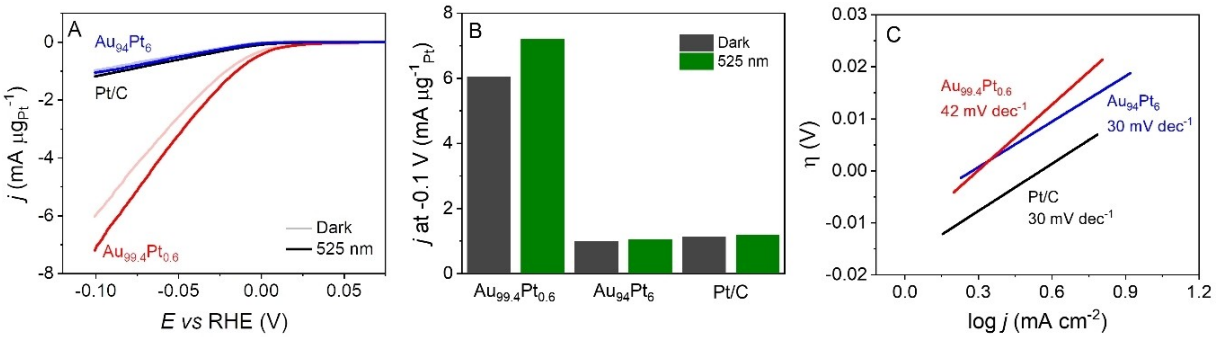

Figure 2. (A) LSV curves normalized by Pt mass for $Au_{94.4}Pt_{0.6}$ and $Au_{99}Pt_6$ NPs (red and blue traces, respectively). The curve for pure Pt NPs is shown for comparison (black trace). Measurements were performed under dark and under 525 nm LED irradiation conditions (dark and LSPR excitation, respectively) and recorded at 5 mVs^{-1} in Ar-saturated 0.5 H_2SO_4. (B) Mass activity comparison for all samples under dark and light irradiation conditions at −0.1 V; and (C) Tafel plots calculated from LSV curves normalized by geometric area (Figure S7A–C) for $Au_{99.4}Pt_{0.6}$ (red trace), $Au_{94}Pt_6$ (blue trace) and Pt/C (black trace).

HER activity of this sample in dark and light excitation conditions.[33] The observed Tafel slopes were the same for LSPR and dark conditions in all catalysts suggesting similar HER mechanisms.[34]

$$\text{Volmer step}: \ H_3O^+ + e^- \rightarrow H_{ads} + H_2O \quad (118\,mV\,dec^{-1}) \tag{1}$$

$$\text{Heyrovsky step}: \ H_{ads} + H_3O^+ + e^- \rightarrow H_2 + H_2O \quad (39\,mV\,dec^{-1}) \tag{2}$$

$$\text{Tafel step}: \ H_{ads} + H_{ads} \rightarrow H_2 \ (30\,mV\,dec^{-1}) \tag{3}$$

Figure S14 suggests a mechanism for the enhanced HER performances in the $Au_{99.4}Pt_{0.6}$ NPs under light illumination based on the generation of LSPR-excited charge carriers.[13,34–36] The chronoamperometry under chopped light illumination (60 s on/off) (Figure S10D) shows a fast increase in current density under light excitation in agreement with the effect of hot carriers on the HER.[34]

DFT calculations on the charge density difference (Figure 3A) for the $Au_{99.4}Pt_{0.6}$ and Au model (Figure S15 and Table S4) revealed a local redistribution of charge at the Pt sites, characterized by areas of electron accumulation (blue) and electron depletion (cyan). This suggests that Pt facili-

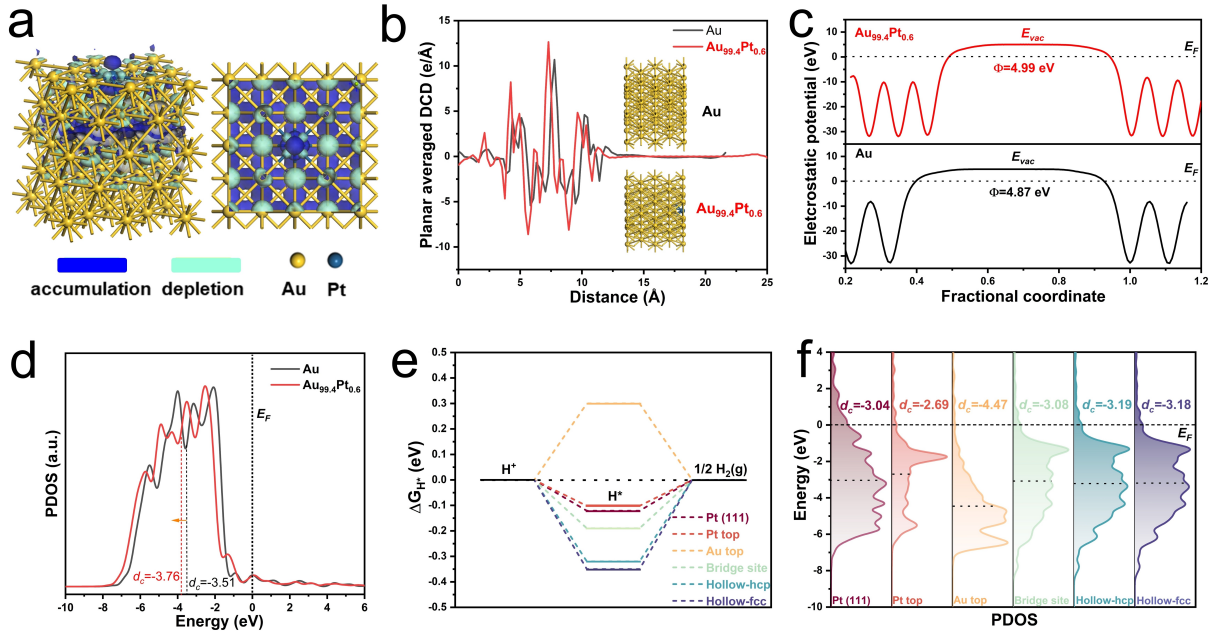

Figure 3. (A) Charge density differences in the constructed $Au_{99.4}Pt_{0.6}$ NPs model (side and top views). The blue and cyan contours represent the regions of electron accumulation and depletion, respectively. (B) The plane-averaged differential charge density (DCD) across the interface, (C) electrostatic potentials, and (D) d-orbital partial density of states (d-PDOS) for Au (black trace) and $Au_{99.4}Pt_{0.6}$ (red trace) model NPs. (E) Gibbs free energy (ΔG_{H^*}) profiles for the HER and (F) d-PDOS on various catalytic sites on Pt (111) and $Au_{99.4}Pt_{0.6}$ (111) surfaces (see Supporting Information for further details).

tates the migration of LSPR-induced hot charges to the Pt or Pt–O sites under light irradiation, leading to higher reaction rates.[37] This could improve the efficient electron transfer to the key adsorbates during the HER, resulting in increased catalytic activity both in the dark and LSPR excitation conditions.

The planar average charge density differences (DCD, Figure 3B) show that the Pt induces a stronger charge redistribution at the interface than pure Au, indicating the formation of an internal electric field. This is supported by the calculated work functions of Au and $Au_{99.4}Pt_{0.6}$ (Figure 3C). The increased work function for $Au_{99.4}Pt_{0.6}$ indicates a lower Femi energy (E_F) level and a larger work function of the AuPt-based shell. The contact between Au and AuPt alloy induces charge redistribution around the interface, enabling electron transfer from Au to AuPt until their work functions become equivalent.[38] Consequently, LSPR-excited hot electrons would gather on the AuPt sites, while holes would be enriched on the Au side, contributing to enhanced performances under LSPR excitation by suppressing their recombination, for example. The projected partial density of states (PDOS) over the d orbitals (Figure 3D) shows that the $Au_{99.4}Pt_{0.6}$ exhibited a lower d band centre (d_c) relative to Au, indicating that Pt leads to modulations in the electronic structure even at low concentration levels.[39]

The hydrogen adsorption free energy (ΔG_{H^*}) for the H* adsorption/desorption step serves as a key descriptor for HER activities. We calculated the ΔG_{H^*} values for various possible adsorption configurations at different catalytic sites (Pt top, Au top, Au–Pt bridge, Au–Au–Pt hollow-hcp, and Au–Au–Pt hollow-fcc sites) over the $Au_{99.4}Pt_{0.6}$ (111) model surface (Figure S16). We also calculated the ΔG_{H^*} values for Pt surface sites on a pure Pt NP model. Figure 3E reveals that several active sites including Pt sites over Pt (111), Pt top sites in $Au_{99.4}Pt_{0.6}$ (111), and Au–Pt bridge sites in $Au_{99.4}Pt_{0.6}$ (111), exhibit low ΔG_{H^*} values (less than 0.20 eV), whereas the ΔG_{H^*} values of Au top and hollow sites are higher. The Pt top sites over $Au_{99.4}Pt_{0.6}$ (111) displayed the lowest ΔG_{H^*} value (−0.10 eV), suggesting that they are the optimum sites to promote H adsorption and catalyse the HER. The PDOS of d orbitals of various catalytic sites and the relative d band centre for the adsorption of active species (H*) show that Pt top sites exhibit a more positive d_c, indicative of promoted H absorption and enhanced HER activity (Figure 3F). These results suggest that the higher HER activity of $Au_{99.4}Pt_{0.6}$ NPs occurs due to the promotion of optimum adsorption/desorption of H* species (under both dark and light conditions) and the facilitation of LSPR-excited charge carrier transfer to the Pt and Pt–O sites (under light excitation). Here, a more dilute distribution of Pt close to the Au surface in the $Au_{99.4}Pt_{0.6}$ NPs can facilitate a more efficient transfer of hot carriers to the Pt-based sites.

The stability of the $Au_{99.4}Pt_{0.6}$ NPs was investigated by performing chronoamperometry experiments to probe the decrease in catalytic activity over time under light irradiation and dark conditions. These results are shown in Figure S17. While the stability was superior to Pt/C under dark conditions (no LSPR excitation), light irradiation led to a higher decrease in activity as compared to Pt/C NPs. To gain further insights into these results, we performed STEM-EDS mapping and TEM imaging on the $Au_{99.4}Pt_{0.6}$ NPs after the HER stability tests (chronoamperometry) under light excitation conditions (Figures S18 and S19, respectively). A change in the Pt distribution on the NPs was detected, in which Pt became more uniformly distributed in the entire extension of NPs rather than being concentrated at the shell (Figure S18). Also, some degree of aggregation was observed, indicating that the stability under light excitation conditions needs to be further optimized (Figure S19).

We next focused on the application of these ultra-low loading antenna-reactor catalysts for the electrocatalytic conversion of NO_2^- to NH_3 (NO_2RR). The cyclic voltammograms for $Au_{99.4}Pt_{0.6}$ and $Au_{94}Pt_6$ NPs in the presence of NO_2^- are characteristic of the reduction of NO_x compounds (Figure 4A and Figure S20, red and blue traces, respectively).[40] Voltammograms in the absence of NO_2^- are shown in Figure S21. Figure 4A is normalized by the mass of Pt, and since $Au_{99.4}Pt_{0.6}$ contains a smaller amount of Pt, its mass-normalized CV presents a significantly higher capacitive current compared to $Au_{94}Pt_6$. However, when we examine the area-normalized CVs (Figure S18), it can be observed that the capacitive current for both catalysts is comparable. To further confirm this, the double-layer capacitance (C_{dl}), which is proportional to the ECSA, was determined by CV in the capacitive region with different scan rates (Figure S20). The data shows that $Au_{99.4}Pt_{0.6}$ and $Au_{94}Pt_6$ exhibited C_{dl} values of the same order of magnitude (0.101 $\mu F cm^{-2}$ and 0.119 $\mu F cm^{-2}$, respectively). Also, by examining the geometric area normalized CVs (Figure S20), the NO2RR activity among the samples seems similar. While the Pt loading in the electrode was similar for the Pt/C and $Au_{94}Pt_6$ electrodes, it was lower for the $Au_{99.4}Pt_{0.6}$. In this case, the detected similar performance in terms of geometric area occurs due to the intrinsic higher catalytic activity of this sample as supported by the Pt mass activity and mass activities considering the total metal loading (Figure S23).

The mass activities at 0.05 V (Figure 4B) show that under both dark and light irradiation conditions, the $Au_{99.4}Pt_{0.6}$ NPs displayed higher activities (6.5 times higher than the $Au_{94}Pt_6$ NPs). While irradiation with visible light led to an enhancement in performance for both samples, the relative increase was again much higher for $Au_{99.4}Pt_{0.6}$ NPs. The mass activities in the dark corresponded to 149 and 23 $\mu A \mu g^{-1}$ for $Au_{99.4}Pt_{0.6}$ and $Au_{94}Pt_6$ NPs, respectively. Plasmonic excitation led to an increase to 366 and 41.5 $\mu A \mu g^{-1}$, respectively (enhancements of 2.5- and 1.8-fold, respectively). As in the HER, the higher activity of the $Au_{99.4}Pt_{0.6}$ NPs can be attributed to the more dilute Pt surface distribution, lower coordination of Pt to other Pt centres, and the presence of Pt–O sites.[41,42] The mass activities in terms of the total metal loading (Au + Pt) are shown in Figure S23. The on–off transients for $Au_{99.4}Pt_{0.6}$ NPs under chopped light excitation at 525 nm (Figure 4C) show fast and reproducible current responses to on–off illumination cycles. Here, tried to mitigate the heat effects by performing all experiments in a temperature-controlled

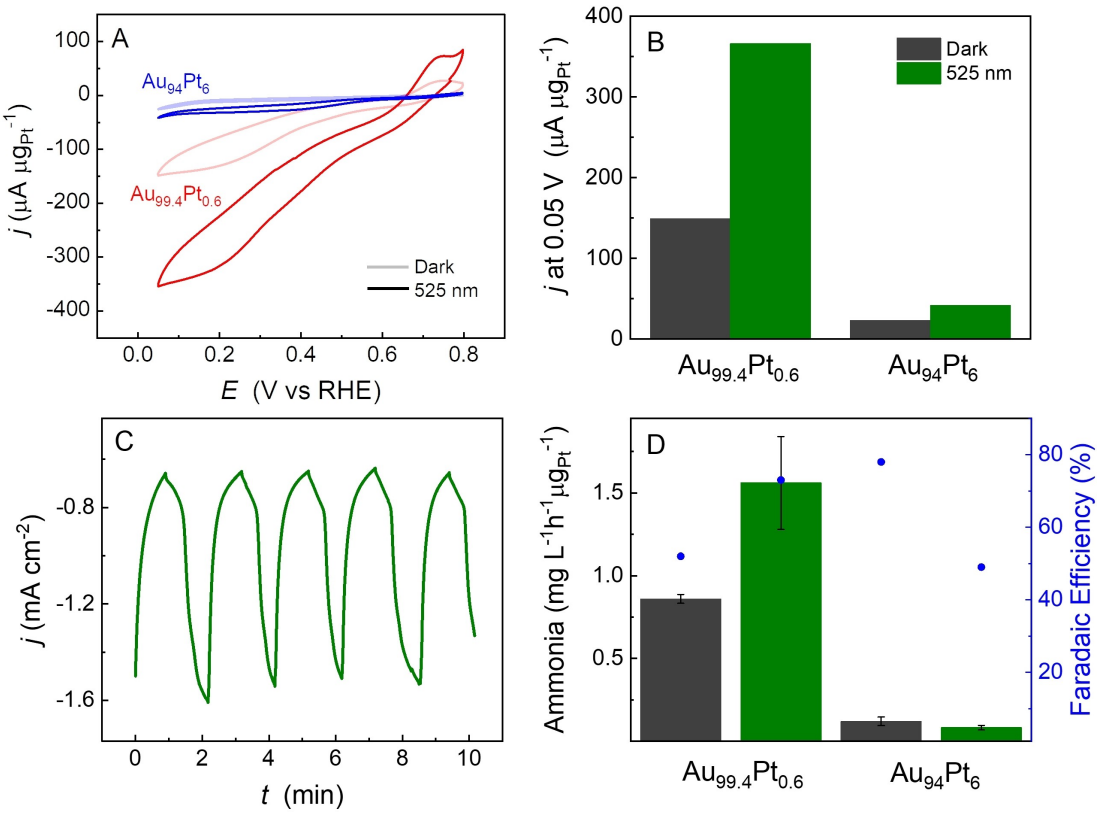

Figure 4. (A) Cyclic voltammograms for $Au_{99.4}Pt_{0.6}$ (red trace) and $Au_{94}Pt_6$ (blue trace) NPs in 0.1 M $HClO_4$ and 10 mM $NaNO_2$ in the dark (shaded line) and under light irradiation conditions (solid line) recorded at 0.010 Vs^{-1}. (B) Bar graph for the mass activity at 0.05 V for $Au_{99.4}Pt_{0.6}$ and $Au_{94}Pt_6$ NPs under dark (black bars) and light irradiation (green bars). (C) Chronoamperometric curves for $Au_{99.4}Pt_{0.6}$ NPs recorded at 0.050 V in 0.1 M $HClO_4$ and 10 mM $NaNO_2$ in on/off conditions under light excitation at 525 nm. (D) The concentration of NH_3 obtained from $Au_{99.4}Pt_{0.6}$ and $Au_{94}Pt_6$ NPs under dark (black bars) and light irradiation (green bars) normalized by the Pt mass. The faradaic efficiencies are illustrated by the blue dots. Light excitation corresponded to 525 nm.

system. Nevertheless, in plasmonic catalysis, the LSPR excitation can lead to localized heating effects, and the untangling of the effect of localized heating and hot charge carriers over activities is difficult to achieve.[43,44] Therefore, is possible that heating and diffusion effects can influence photoresponses. It is important to note that it has been reported that the local temperature at the electrocatalyst/medium interface under laser irradiation from 0 to 2.55 W/cm^2 (more intense than our LED source) was only moderately higher than that under dark conditions and that the temperature increase resulting from photothermal heating has low influence on the HER performances.[45]

The reduction of NO_2^- to NH_3 can lead to several products as shown in Figure S24. To investigate reaction selectivity, we quantified the amount of produced NH_3 as shown in Figure 4D (more information in SI, Figure S25 and S26) by the indophenol method. The plasmonic enhancement increased the selectivity towards NH_3 formation for the $Au_{99.4}Pt_{0.6}$ NPs from 0.86 in the dark to 1.56 $mgL^{-1}h^{-1}μg_{Pt}^{-1}$ under light excitation, whereas the selectivity to NH_3 remained nearly unchanged for the $Au_{94}Pt_6$ NPs. Here, it is plausible that a more dilute concentration of Pt in the shell can increase the light absorption and the transfer of hot carriers to the Pt-based sites, leading to enhanced activities and thus favouring the greater formation of NH_3 (corresponding to a larger extent of reduction relative to the other products). Also, the Pt sites with lower coordination numbers and Pt–O bonds on the $Au_{99.4}Pt_{0.6}$ NPs (as shown by our spectroscopic data) could be responsible for the fast hydrogenation to NH_3, as these sites have a lower energy barrier to H_2 production than metallic Pt sites.[46,47] Since Pt/C is not a benchmark catalyst for NO_2RR, the activities were not benchmarked against commercial Pt/C. In this case, rather than benchmarking the performances, our goal was to focus on the tuning of surface composition on the reaction selectivity under light excitation due to plasmonic effects. It is important to note that the single-compartment cell design employed in our studies (Scheme S1) can lead to ammonia oxidation at the counter electrode, underestimating the true ammonia yield. Nevertheless, a clear increase in selectivity could be detected under light irradiation. The calculated Faraday efficiencies illustrate a relation between the current passing through the sample and the ammonia formation to address this challenge. The observed enhancement in selectivity, even with the acknowledged limitation, supports the conclusion that plasmonic excitation leads to an enhancement in selectivity towards NH_3. Finally, the chro-

noamperometry curves to assess the stability of the $Au_{99.4}Pt_{0.6}$ and $Au_{94}Pt_6$ NPs for the NO2RR under light irradiation conditions are shown in Figure S27. Both samples displayed relatively good stability under our employed conditions, with a slight increase in performance as a function of time.

Figure 5 shows DFT calculations of the charge density differences for NO adsorbed on Pt in the $Au_{99.4}Pt_{0.6}$ model. NO adsorption resulted in strong local charge redistribution over the active sites, causing electron density migration from the surface to the adsorbed *NO species (supported by quantitative Mulliken charge analysis). The PDOS following NO adsorption (Figure 5B) shows a downshifting in the energy of the 2p orbitals of *NO relative to free NO because of surface interaction. Our simulation also reveals that the 2p antibonding orbital is located close to the E_F and therefore can by LSPR excited charge carriers, leading to enhanced reaction rates under plasmonic excitation. Moreover, the adsorption energies of NO on $Au_{99.4}Pt_{0.6}$ (111) (Figure 5C) were significantly larger than those on Au, indicating that the presence of Pt, even at dilute concentrations, modulates this energy.

The calculated adsorption Gibbs free energy of various intermediates during NO_2RR is presented in Figure 5D. For Au, Pt and $Au_{99.4}Pt_{0.6}$ NPs models, the protonation of *NO to *NHO was identified as the rate-determining step (RDS) in which $Au_{99.4}Pt_{0.6}$ displayed the lowest energy barrier of 0.25 eV, which can be further decreased under LSPR excitation.[3] $Au_{99.4}Pt_{0.6}$ also required the lowest free energy to release $*NH_3$ from the catalyst surface (Figure 5C), further contributing to the higher catalytic activities. Thus, both the electronic structure and the interaction with LSPR excitation contributed to the excellent NO_2RR activity and selectivity towards NH_3 of $Au_{99.4}Pt_{0.6}$ NPs.

Conclusions

Ultralow loadings and non-uniform surface segregation of Pt at the surface of Au in $Au_{99.4}Pt_{0.6}$ NPs are shown to provide excellent catalytic performance and selectivity for the HER and NO_2RR reactions, with the performance being further enhanced under visible light excitation. Although AuPt NPs with higher Pt loading provided superior performance

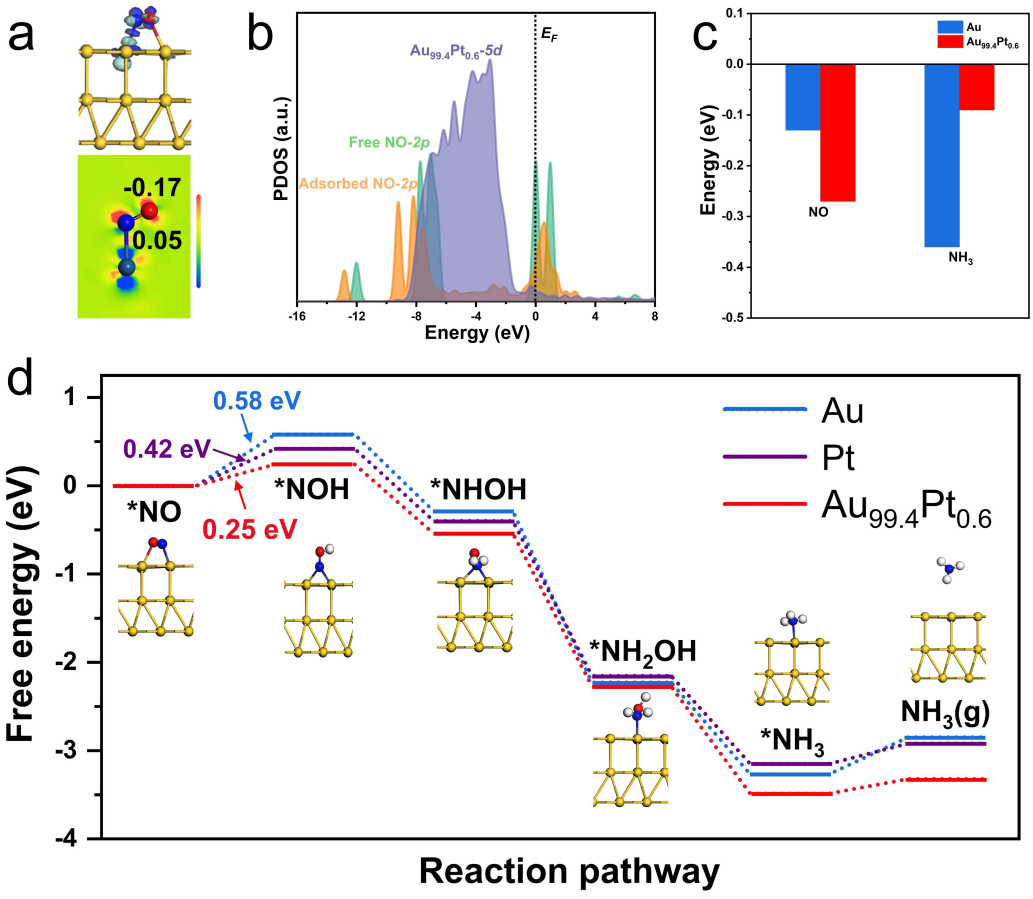

Figure 5. (A) Charge density differences and Mulliken charge analysis in the constructed $Au_{99.4}Pt_{0.6}$ NPs model containing a NO molecule adsorbed at the Pt top site. The cyan and blue contours represent the regions of electron accumulation and depletion, respectively. For 2D maps, the scale from red to blue was 0.1 to −0.1 e. (B) PDOS for a free (green) and adsorbed (orange) NO molecule (2p levels) at the Pt top site in the $Au_{99.4}Pt_{0.6}$ NPs model. (C) Adsorption energies of NO and NH_3 on Au (111) and $Au_{99.4}Pt_{0.6}$ (111) model NPs surfaces. (D) Free energy profiles for the NO_2RR pathway on the Au, Pt, and $Au_{99.4}Pt_{0.6}$ NPs model. The overall reaction trends were downhill on the built models.

compared to commercial Pt/C catalysts, the best catalytic properties were achieved at the lowest $Au_{99.4}Pt_{0.6}$ content: including a 6-fold increase in the HER relative to Pt, a 6.5-fold increase in the nitrite reduction relative to $Au_{94}Pt_6$, and a 1.8-fold increase in the selectivity for the formation of NH_3. Density functional theory calculations showed that dilute Pt sites and intimate contact between Pt-rich and Au-rich regions at the surface facilitate the formation of electron-rich hot-carrier puddles associated with the Pt-based surface sites, accelerating the reactions. Our results motivate further study of the potential of ultra-low metal loadings when seeking to synthesize plasmonic catalysts with improved performances and control over reaction selectivity under visible light excitation.

Acknowledgements

This work was supported by the Jane and Aatos Erkko Foundation, the Academy of Finland (decision number 350208), and seed funding from the Helsinki Institute of Sustainability Science (HELSUS). SJH acknowledges funding from EPSRC (EP/P009050/1) and the European Research Council under the Horizon 2020 programme for the ERC Starter Grant EvoluTEM (715502). TEM access for this work was supported by the Henry Royce Institute for Advanced Materials, funded through EPSRC grants EP/R00661X/1, EP/S019367/1, EP/P025021/1, and EP/P025498/1. ES thanks the Sao Paulo Research Foundation (FAPESP, #2013/07296-2, #2017/11986-5) and Brazilian Council for Scientific and Technological Development (CNPq, 405752/2022-9) for financial support (310550/2022-0). HS acknowledges Prof. Marko Huttula and Strategic Research Council within the Research Council of Finland decision 358422, JustH2Transit for funding support. EU/Interreg Aurora/Sustainable Hydrogen project is also acknowledged for its financial support. This work was partly supported by the European Union Horizon 2020 research and innovation program under the NOMATEN Teaming grant (857470) and the European Regional Development Fund via the Foundation for Polish Science International Research Agenda PLUS program grant (MAB PLUS/2018/8). The publication was created partly within the framework of the project of the Minister of Science and Higher Education "Support for the activities of Centres of Excellence established in Poland under Horizon 2020″ under contract no. MEiN/2023/DIR/3795. Part of the research described in this work was performed at the Canadian Light Source, a national research facility of the University of Saskatchewan, which is supported by the Canada Foundation for Innovation (CFI), the Natural Sciences and Engineering Research Council (NSERC), the National Research Council (NRC), the Canadian Institutes of Health Research (CIHR), the Government of Saskatchewan, and the University of Saskatchewan. We thank Dr. Graham King for the synchrotron XRD data collection. We thank Graham Hutchings for his comments on the manuscript.

Conflict of Interest

The authors declare no conflict of interest.

Data Availability Statement

The data that support the findings of this study are available from the corresponding author upon reasonable request.

Keywords: Antenna-reactor nanoparticles · plasmonic catalysis · surface plasmon resonance · hydrogen evolution · nitrite reduction

[1] X. Tao, Y. Zhao, S. Wang, C. Li, R. Li, *Chem. Soc. Rev.* **2022**, *51*, 3561–3608.
[2] Y. Wang, C. Wang, M. Li, Y. Yu, B. Zhang, *Chem. Soc. Rev.* **2021**, *50*, 6720–6733.
[3] E. Contreras, R. Nixon, C. Litts, W. Zhang, F. M. Alcorn, P. K. Jain, *J. Am. Chem. Soc.* **2022**, *144*, 10743–10751.
[4] W. Liao, J. Wang, G. Ni, K. Liu, C. Liu, S. Chen, Q. Wang, Y. Chen, T. Luo, X. Wang, Y. Wang, W. Li, T.-S. Chan, C. Ma, H. Li, Y. Liang, W. Liu, J. Fu, B. Xi, M. Liu, *Nat. Commun.* **2024**, *15*, 1264.
[5] J. Zhu, L. Hu, P. Zhao, L. Y. S. Lee, K.-Y. Wong, *Chem. Rev.* **2020**, *120*, 851–918.
[6] P. H. van Langevelde, I. Katsounaros, M. T. M. Koper, *Joule* **2021**, *5*, 290–294.
[7] J. Han, X. Meng, L. Lu, Z. L. Wang, C. Sun, *Nano Energy* **2020**, *72*, 104669.
[8] Y. Chao Hu, Y. Zhi Wang, R. Su, C. Rong Cao, F. Li, C. Wen Sun, Y. Yang, P. Fei Guan, D. Wei Ding, Z. Lin Wang, W. Hua Wang, Y. C. Hu, C. R. Cao, D. W. Ding, W. H. Wang, Y. Yang, Y. Z. Wang, C. W. Sun, Z. L. Wang, F. Li, R. Su, P. F. Guan, *Adv. Mater.* **2016**, *28*, 10293–10297.
[9] Y. C. Hu, C. Sun, C. Sun, *ChemCatChem* **2019**, *11*, 2401–2414.
[10] P. H. C. Camargo, E. Cortés, *Plasmonic Catalysis*, Wiley **2021**.
[11] L. Yuan, J. Zhou, M. Zhang, X. Wen, J. M. P. Martirez, H. Robatjazi, L. Zhou, E. A. Carter, P. Nordlander, N. J. Halas, *ACS Nano* **2022**, *16*, 17365–17375.
[12] S. Linic, P. Christopher, D. B. Ingram, *Nat. Mater.* **2011**, *10*, 911–921.
[13] T. P. Araujo, J. Quiroz, E. C. M. Barbosa, P. H. C. Camargo, *Curr. Opin. Colloid Interface Sci.* **2019**, *39*, 110–122.
[14] Y. Li, Z. Li, C. Chi, H. Shan, L. Zheng, Z. Fang, *Adv. Sci.* **2017**, *4*, 1600430.
[15] A. G. M. da Silva, T. S. Rodrigues, J. Wang, P. H. C. Camargo, *Chem. Commun.* **2022**, *58*, 2055–2074.
[16] M. L. Brongersma, N. J. Halas, P. Nordlander, *Nat. Nanotechnol.* **2015**, *10*, 25–34.
[17] E. Cortés, L. V. Besteiro, A. Alabastri, A. Baldi, G. Tagliabue, A. Demetriadou, P. Narang, *ACS Nano* **2020**, *14*, 16202–16219.
[18] J. Quiroz, E. C. M. Barbosa, T. P. Araujo, J. L. Fiorio, Y.-C. Wang, Y.-C. Zou, T. Mou, T. V. Alves, D. C. de Oliveira, B. Wang, S. J. Haigh, L. M. Rossi, P. H. C. Camargo, *Nano Lett.* **2018**, *18*, 7289–7297.
[19] Y. Dong, C. Hu, H. Xiong, R. Long, Y. Xiong, *ACS Catal.* **2023**, 6730–6743.
[20] J. Boltersdorf, A. C. Leff, G. T. Forcherio, D. R. Baker, *Crystals (Basel)* **2021**, *11*, 226.
[21] A. Joplin, S. A. Hosseini Jebeli, E. Sung, N. Diemler, P. J. Straney, M. Yorulmaz, W.-S. Chang, J. E. Millstone, S. Link, *ACS Nano* **2017**, *11*, 12346–12357.

[22] J. Quiroz, P. F. M. de Oliveira, S. Shetty, F. E. Oropeza, V. A. de la Peña O'Shea, L. C. V. Rodrigues, M. P. de S Rodrigues, R. M. Torresi, F. Emmerling, P. H. C. Camargo, *ACS Sustainable Chem. Eng.* **2021**, *9*, 9750–9760.
[23] L. Zhou, J. M. P. Martirez, J. Finzel, C. Zhang, D. F. Swearer, S. Tian, H. Robatjazi, M. Lou, L. Dong, L. Henderson, P. Christopher, E. A. Carter, P. Nordlander, N. J. Halas, *Nat. Energy* **2020**, *5*, 61–70.
[24] U. Aslam, S. Chavez, S. Linic, *Nat. Nanotechnol.* **2017**, *12*, 1000–1005.
[25] C. Engelbrekt, K. T. Crampton, D. A. Fishman, M. Law, V. A. Apkarian, *ACS Nano* **2020**, *14*, 5061–5074.
[26] S. Chavez, U. Aslam, S. Linic, *ACS Energy Lett.* **2018**, *3*, 1590–1596.
[27] C. H. Choi, M. Kim, H. C. Kwon, S. J. Cho, S. Yun, H.-T. Kim, K. J. J. Mayrhofer, H. Kim, M. Choi, *Nat. Commun.* **2016**, *7*, 10922.
[28] P. N. Duchesne, Z. Y. Li, C. P. Deming, V. Fung, X. Zhao, J. Yuan, T. Regier, A. Aldalbahi, Z. Almarhoon, S. Chen, D. Jiang, N. Zheng, P. Zhang, *Nat. Mater.* **2018**, *17*, 1033–1039.
[29] T. Chao, Y. Hu, X. Hong, Y. Li, *ChemElectroChem* **2019**, *6*, 289–303.
[30] N. J. Zaluzec, *Thin Solid Films* **1980**, *72*, 177–192.
[31] Gatan Inc., "Electron energy loss spectroscopy (EELS) Atlas [Online]. Available at: https://eels.info/atlas/gold (Accessed: March 2023))," **n.d**.
[32] X. Tian, P. Zhao, W. Sheng, *Adv. Mater.* **2019**, *31*, 1808066.
[33] H. Yang, Y. Ji, Q. Shao, W. Zhu, M. Fang, M. Ma, F. Liao, H. Huang, Y. Zhang, J. Yang, Z. Fan, Y. Li, Y. Liu, M. Shao, Z. Kang, *Energy Environ. Sci.* **2023**, *16*, 574–583.
[34] A. J. Wilson, V. Mohan, P. K. Jain, *J. Phys. Chem. C* **2019**, *123*, 29360–29369.
[35] H.-X. Zhang, Y. Li, M.-Y. Li, H. Zhang, J. Zhang, *Nanoscale* **2018**, *10*, 2236–2241.
[36] J. Mo, E. C. M. Barbosa, S. Wu, Y. Li, Y. Sun, W. Xiang, T. Li, S. Pu, A. Robertson, T. Wu, Y. Soo, T. V. Alves, P. H. C. Camargo, W. Kuo, S. C. E. Tsang, *Adv. Funct. Mater.* **2021**, *31*, 2102517.
[37] T. Dai, X. Zhang, M. Sun, B. Huang, N. Zhang, P. Da, R. Yang, Z. He, W. Wang, P. Xi, C.-H. Yan, *Adv. Mater.* **2021**, *33*, 2102593.
[38] Y. Wang, J. Hu, T. Ge, F. Chen, Y. Lu, R. Chen, H. Zhang, B. Ye, S. Wang, Y. Zhang, T. Ma, H. Huang, *Adv. Mater.* **2023**, *n/a*, 2302538.
[39] R. Zhang, Y. Guo, S. Zhang, D. Chen, Y. Zhao, Z. Huang, L. Ma, P. Li, Q. Yang, G. Liang, C. Zhi, *Adv. Energy Mater.* **2022**, *12*, 2103872.
[40] K. N. da Silva, G. Soffiati, E. Z. da Silva, M. A. San-Miguel, E. Sitta, *New J. Chem.* **2022**, *46*, 12132–12138.
[41] Q. Ge, M. Neurock, *J. Am. Chem. Soc.* **2004**, *126*, 1551–1559.
[42] G. L. Beltramo, M. T. M. Koper, *Langmuir* **2003**, *19*, 8907–8915.
[43] L. Zhou, D. F. Swearer, C. Zhang, H. Robatjazi, H. Zhao, L. Henderson, L. Dong, P. Christopher, E. A. Carter, P. Nordlander, N. J. Halas, *Science* **2018**, *362*, 69–72.
[44] S. Singh, R. Verma, N. Kaul, J. Sa, A. Punjal, S. Prabhu, V. Polshettiwar, *Nat. Commun.* **2023**, *14*(1), 1–18.
[45] A. J. Wilson, V. Mohan, P. K. Jain, *J. Phys. Chem. C* **2019**, *123*, 29360–29369.
[46] F.-Y. Yu, Z.-L. Lang, L.-Y. Yin, K. Feng, Y.-J. Xia, H.-Q. Tan, H.-T. Zhu, J. Zhong, Z.-H. Kang, Y.-G. Li, *Nat. Commun.* **2020**, *11*, 490.
[47] H. Yang, Y. Ji, Q. Shao, W. Zhu, M. Fang, M. Ma, F. Liao, H. Huang, Y. Zhang, J. Yang, Z. Fan, Y. Li, Y. Liu, M. Shao, Z. Kang, *Energy Environ. Sci.* **2023**, *16*, 574–583.

Manuscript received: March 20, 2024
Accepted manuscript online: May 6, 2024
Version of record online: June 14, 2024